1

2

Cryo-EM structures reveal how ATP and DNA binding in MutS coordinate the sequential steps of DNA mismatch repair

5

6

Alessandro Borsellini[1], Vladislav Kunetsky[2], Peter Friedhoff[2], Meindert H. Lamers[1]

8

[1]Department of Cell and Chemical Biology, Leiden University Medical Center, Leiden, The Netherlands. [2]Institute for Biochemistry, Justus-Liebig University, Giessen, Germany.

11

Correspondence should be addressed to m.h.lamers@lumc.nl

13

Abstract (186 of max 200)

DNA mismatch repair detects and removes mismatches from DNA reducing the error rate of DNA replication a 100-1000 fold. The MutS protein is one of the key players that scans for mismatches and coordinates the repair cascade. During this, MutS undergoes multiple conformational changes that initiate the subsequent steps, in response to ATP binding, hydrolysis, and release. How ATP induces the different conformations in MutS is not well understood. Here we present four cryo-EM structures of *Escherichia coli* MutS at sequential stages of the ATP hydrolysis cycle. These structures reveal how ATP binding and hydrolysis induces a closing and opening of the MutS dimer, respectively. Additional biophysical analysis furthermore explains how DNA binding modulates the ATPase cycle by preventing hydrolysis during scanning and mismatch binding, while preventing ADP release in the sliding clamp state. Nucleotide release is achieved when MutS encounters single stranded DNA that is produced during the removal of the daughter strand. This way, the combination of the ATP binding and hydrolysis and its modulation by DNA enable MutS to adopt different conformations needed to coordinate the sequential steps of the mismatch repair cascade.

Introduction

DNA mismatch repair is an evolutionary conserved mechanism that removes mispaired bases from the DNA after DNA replication. Doing so, it reduces the mutation frequency a 100 to a 1000-fold, preventing cancer and drug resistance. It also plays roles in regulation of recombination, triplet repeat expansion and DNA damage signalling [1,2]. The repair process consists of a cascade of proteins that act sequentially. The MutS protein scans the DNA for mismatches, and upon recognition recruits a second protein MutL. In *Escherichia coli* (*E. coli*), MutL subsequently activates the endonuclease MutH that creates a nick in the newly synthesized strand on hemi-methylated GATC sites [3-5]. In other species, including eukaryotes, the endonuclease activity resides in the MutL homologs themselves [6,7] and is directed to the newly synthesized strand by the DNA sliding clamp (β or PCNA) [8,9]. In bacteria, the single stranded nick then forms the entry point for the UvrD helicase, or RecD2 in some Bacillus species [10,11], that with the aid of a 5'-3' or 3'-5' exonuclease will excise the newly synthesized strand [12,13]. The removed stretch of DNA will then be resynthesized by a DNA polymerase and the remaining nick sealed by a DNA ligase [14]. In the eukaryotic system the strand removal process is less well understood but involves the replicative DNA polymerase δ and exonuclease EXO1 [15].

Throughout this process, MutS is the master coordinator that initiates the subsequent steps of the repair cascade. First, it scans the genome in search for a mismatch. Once it is bound to a mismatch it undergoes a conformational change into a sliding clamp that recruits the second protein MutL [16,17]. In the clamp state, MutS remains on the DNA for prolonged times and only releases the DNA when it encounters a DNA ends [18,19] or a ssDNA gap [20,21]. This way, MutS molecules will remain present on the DNA until the mismatch has been removed and the repair process is terminated. Recently we have determined multiple cryo-EM structures of MutS on DNA at different stages of the repair process, revealing the multiple conformations that enable

57   it to perform its different tasks [22]. ATP binding and hydrolysis are essential for MutS to switch

58   between the different states [23], but the molecular basis of these transitions and how they are

59   regulated remains unresolved. To gain insight into the ATP-induced conformational changes

60   in MutS we determined four structures of apo MutS at sequential stages of the ATP hydrolysis

61   cycle: ADP-bound, ATP-bound, bound to a non-hydrolysable ATP analogue AMPPNP and

62   bound to the transition state analogue ADP-vanadate [24] (ADP-VO$_4^{3-}$ / ADP-Vi). These

63   structures show how an open MutS dimer in the ADP-bound form closes upon binding to a

64   single ATP but does not reach a hydrolysis competent active site in this structure. Only upon

65   binding of two triphosphate nucleotides the complete active site is formed that can hydrolyse

66   ATP.

67   Additional biochemical analysis combined with the recently determined structures of DNA-

68   bound MutS, explains how ATP and DNA binding work together to initiate the subsequent

69   steps of the repair cascade. During both the scanning of the DNA as well as mismatch binding,

70   the DNA keeps the ATPase domains in an open, non-catalytic state where the nucleotide

71   binding sites are free to exchange ADP for ATP. Two ATP molecules are needed to transform

72   MutS into the sliding clamp conformation that recruits MutL. In this clamp state, the ATPase

73   active sites are completed and can hydrolyse ATP. However, the dsDNA itself keeps the

74   nucleotide binding sites closed and prevents nucleotide release until MutS reaches a stretch of

75   ssDNA where the interactions with the dsDNA are lost. This enables the dimer to open up and

76   reset the ATPase site for a new round of ATP and DNA binding.

77

78   **Results**

79   **Structures apo MutS at sequential stages of the ATP hydrolysis cycle**

80   In order to gain insight into the mechanism of ATP hydrolysis in MutS, we determined four

81   cryo-EM structures of the MutS dimer in absence of DNA at sequential stages of the hydrolysis

82   cycle: 1) bound to two ADP molecules, 2) bound to one ADP and one ATP, 3) bound to two

83   AMPPNP molecules, a non-hydrolysable ATP analogue, and 4) bound to two ADP-vanadate

84   (ADP-Vi) molecules, a transition state analogue (Fig. 1, Table 1, and Extended Data Figs. 1-

85   4). The four structures were determined to a resolution of 4.8, 3.3, 3.4, and 3.7 Å, respectively.

86   All structures were obtained by incubating 4 μM MutS with 3 mM of the nucleotide for 5 min

87   at 4 °C in buffer containing Mg^{2+} before plunge freezing in liquid ethane. In the resulting cryo-

88   EM data, we find that three of the four conditions show a single conformational state: an open

89   form for ADP_2 and a closed form for both $AMPPNP_2$ and ADP-Vi_2. In contrast, in the sample

90   incubated with ATP we observe both the open ADP_2-bound form and the closed ATP:ADP-

91   bound form indicating that under these conditions MutS can hydrolyse ATP.

92   In all four structures, the clamp domains are poorly resolved, indicating that in the absence

93   of DNA these domains are flexible. The flexibility is most pronounced in the structure of ADP-

94   bound MutS, where the lever and clamp domains adopt different conformations that can be

95   discerned by negative stain electron microscopy (Fig 1i). The four structures show an

96   increasing compaction going from the open form in the ADP_2-bound state, to ATP:ADP-bound

97   state, to the most compact form in the $AMPPNP_2$ and ADP-Vi_2-bound state that both adopt an

98   identical conformation. The transition from the ADP_2-bound to ATP:ADP-bound is

99   characterized by a 35° rotation of the two monomers towards each other around a pivot point

100   located at the interface of the two ATPase domains (Fig. 1j-k, Supplementary Video 1). It is

101   noteworthy that the addition of a single PO_4^{3-} ion (from ADP to ATP) results in a dramatic

102   increase in resolution, from 4.8 to 3.3 Å, due to the more stable conformation MutS adopts in

103   the ATP-bound form. The ATP:ADP to $AMPPNP_2$/ADP-Vi_2 transition is the result of an

104   additional ~6° twist of the ATPase domains along the axis of the helix at the bottom of the

105   ATPase domain (Fig. 1l), resulting in a further closing of the nucleotide binding site

106   (Supplementary Video 1-2). This second rotation would result in a clash of the mismatch-

107   binding domains of the two monomers (Fig. 1m), which may be the reason that the connector-

108   and mismatch domains in one of the two monomers rotate towards the ATPase domains (Fig.

109   1n, Supplementary Video 3). This rotation is identical to that observed in the ATP-induced

110   DNA-bound, clamp state MutS [22,25]. However, in clamp state MutS both monomers have

111   rotated the connector and mismatch domains. Of the four structures, only the ADP-bound state

112   is compatible with DNA binding, as the closing of the lever domains in the ATP and

113   AMPPNP/ADP-Vi bound structures blocks the entry channel for the DNA. This suggests that

114   both monomers need to have hydrolysed ATP before MutS can bind DNA.

115

116   **Closing of the MutS dimer completes the ATPase active site for hydrolysis**

117   Like all ABC ATPases, the MutS ATPase domains are composite active sites where residues

118   from both monomers are required for ATP hydrolysis [26]. The four structures presented in this

119   work illustrate how the two ATPase domains of both monomers come together to complete the

120   MutS active site during ATP hydrolysis (Fig. 2a). The completion of the ATPase active site is

121   driven by the negative charge of the γ-phosphate in ATP that forms an attractive force to the

122   positive charge of the helix dipole [27] that is deposited via a serine (Ser668 in MutS) in the

123   opposing monomer [28] (Fig. 1j-k, 2f). In the open, ADP_2-bound form, the nucleotide is exposed

124   and free to exchange with ATP molecules from solution (Fig. 2b). In contrast, in the closed

125   ATP:ADP-bound and $AMPPNP_2/ADP-Vi_2$-bound structures the nucleotides in both monomers

126   are encapsulated and likely slowed down in leaving the active site (Fig. 2c).

127   In the ATP-bound site of the ATP:ADP structure the signature motif (GxSTF, residues 666-

128   670) [29] of the opposing monomer is further away from the tri-phosphate tail when compared to

129   the structure with AMPPNP and ADP-Vi (Fig. 2a). In addition, only weak density for Mg^{2+} is

130   observed, indicative of a low occupancy (Fig. 2d). In contrast, in the structures of

131    $AMPPNP_2$/ADP-Vi_2-bound MutS the signature loop has moved closer to the phosphate tail of

132   the nucleotide in the opposing monomer and aids in the coordination of the magnesium ion that

133   shows well-defined density (Fig. 2d-f). These two states of the nucleotide binding site (e.g., a

134   sub-optimal conformation in the ATP:ADP state and an optimal conformation in the $AMPPNP_2$

135   and ADP-Vi_2 state) may be the reason for the bi-phasic ATP hydrolysis rate observed in stop-

136   flow experiments on *E. coli* and *Thermus aquaticus* (Taq) MutS. Here an initial burst of

137   ATPase activity is followed by a slower steady state activity [30,31]. It is possible that these two

138   rates represent an initial double ATP occupancy of the nucleotide binding sites that are optimal

139   for hydrolysis, followed by a slower rate that may be caused by an asymmetric occupancy

140   (ADP:ATP) that is less optimal for hydrolysis and dictated by the alternating ATPase domains

141   [32].

142   The active site conformation of the $AMPPNP_2$ and ADP-Vi_2 structures are identical except

143   for the position of the γ-phosphate that in the ADP-Vi_2 structure is replaced by the VO_4^{3-} ion

144   that adopts a pentavalent coordination and has moved away from the β-phosphate, mimicking

145   a post-hydrolysis transition state (Fig. 2d). As the $AMPPNP_2$/ADP-Vi_2 structures represent the

146   hydrolysis competent form, we will discuss the nucleotide binding site in these structure in

147   more detail. The adenosine moiety of the nucleotide is held in place by Phe596 of monomer A

148   ($Phe596^A$) and $His760^A$ that stack on the base, while $Asp616^A$, $Lys620^A$ and $Thr622^A$ of the

149   Walker A motif (P-loop, residues 614-622) bind the phosphate tail. The Mg^{2+} is coordinated

150   by oxygens of the β- and γ- phosphate of ATP^A and $Ser621^A$. The three water molecules that

151   complete the octahedral coordination of Mg^{2+} that are observed in the crystal structure of MutS

152   bound to a mismatch and ATP [33] are not defined in the cryo-EM maps but are compatible with

153   the position of $Asp693^A$ and Asp661 from monomer B ($Asp661^B$, Fig. 2e-f). $Asp661^B$ can

154   complement the nucleotide binding site of monomer A due to the closing of the MutS dimer

155   that also brings Ser668[B] in close proximity of the γ-phosphate of ATP[A]. Ser668 is part of the

156   signature motif found in ABC ATPases (sequence GxSTF [29]) and located immediately

157   upstream of a helix that is pointed with its N-terminus towards the nucleotide in the opposite

158   monomer. This helix deposits the positive charge of its helix dipole onto the negatively charged

159   phosphate tail of the nucleotide through Ser668[B] (Fig. 2f). With the reduced charge on the

160   phosphate tail and the proper coordination of the Mg^{2+}, an activated water molecule can

161   perform a nucleophilic attack on the γ-phosphate. It has been proposed that in the ABC ATPase

162   Rad50, the equivalent of histidine 728[A] can activate a water molecule to perform the

163   nucleophilic attack on the γ-phosphate [34]. This was corroborated by recent quantum mechanical

164   and molecular mechanical modelling of the ABC transporter HlyB [35]. Accordingly, in our

165   structure His728 is well positioned to activate a water molecule as it is pointing towards the γ-

166   phosphate of AMPPNP. Mutation of any of the residues in the ATP active site described above

167   results in a reduction or loss of ATPase activity (see Table 2).

168

169   Two ATP molecules are needed to bring about clamp-state MutS

170   The structures of $AMPPNP_2$-bound and $ADP-Vi_2$-bound MutS show a large conformational

171   change of the mismatch and connector domain in one of the monomers (Fig. 1n) that is identical

172   to the conformational change observed in clamp-state MutS [22,36]. In the ATP:ADP-bound

173   structure however, this conformational change is absent suggesting that a single ATP bound in

174   the MutS dimer is not sufficient to generate enough force to displace the mismatch and

175   connector domains, which is consistent with the observation that in yeast MSH2-MHS6, both

176   monomers need to bind ATP to transform it into a DNA sliding clamp [37]. To determine if this

177   is indeed the case, we measured the Förster resonance energy transfer (FRET) signal between

178   two fluorophores located on the connector domain (residue 246) of one monomer and on the

179   ATPase domain (residue 798) of the opposing monomer (Fig. 3). Rotation of the connector

180   domain reduces the distance between these two residues and consequently will increase the

181   energy transfer between the two fluorophores. In the presence of ADP, we observe a low FRET

182   signal as predicted from the distance in the ADP-bound structure (Fig 3). Similarly, in the

183   presence of ATP there is no increase in the FRET signal. In contrast, using the non-

184   hydrolysable analogue AMPPNP we observe an increase in the FRET signal as expected from

185   the predicted rotation of the mismatch and connector domain observed in the AMPPNP-bound

186   structures.

187   In the presence of mismatched DNA and ADP, we observe an increase in the FRET signal,

188   possibly due the reduced flexibility of MutS on DNA, compared to apo MutS that is highly

189   flexible in absence of DNA (Fig. 1i). In the presence of mismatched DNA and ATP, we observe

190   a strong increase of the FRET signal, brought about by the formation of clamp state MutS in

191   which the mismatch and connector domains of both monomers have moved closer to the

192   ATPase domains [22,25]. In the presence of DNA and AMPPNP we also observe an increase in

193   the FRET signal, although not as strong, possibly due to DNA-free MutS dimers that in the

194   presence of AMPPNP are prevented from binding DNA (Fig. 1n).

195   Taken together, these results indicate that in the absence of DNA during steady state

196   hydrolysis the MutS dimer binds only one ATP, consistent with the alternating ATPase

197   domains of MutS that have been observed in multiple species [32,38,39] and the slow steady state

198   ATP hydrolysis rate [40]. The single ATP occupancy in the MutS dimer is not enough to bring

199   about a conformational change. This is also observed in mismatch bound MutS that can exist

200   with a single nucleotide triphosphate bound, but not with two [41]. Concurrently, in the cryo-EM

201   structure of clamp-state MutS, both monomers contain nucleotide triphosphate in their

202   nucleotide binding site [22]. Moreover, the binding to DNA may actually promote the binding

203   two ATP molecules that are needed to induce the conformational change into the clamp state:

204   the structures of MutS bound to homoduplex and mismatched DNA show the open

205   conformation of the ATPase domains [22] that allows for the free exchange with ATP, giving

206   MutS the possibility to load two ATP molecules. This is consistent with the fast release of ADP

207   from mismatch-bound MutS, but not from free MutS [17,42]

208

In clamp state MutS, dsDNA prevents nucleotide release from the ATPase active site

210   Upon mismatch and ATP binding, MutS transform into the sliding clamp, that remains

211   trapped on the DNA but can freely slide on the DNA until it reaches a stretch of ssDNA or a

212   double strand break where it can dissociate [18-21]. How MutS is able to remain in the clamp state

213   on DNA for prolonged periods is not known. One possibility is that ATP cannot be hydrolysed

214   in the clamp state, thus keeping MutS in a closed state. However, comparison of the recent

215   structure of clamp state MutS on DNA [22] reveals that the position of the ATPase domains is

216   identical to that found in our ADP-Vi$_2$ structure, which mimics a post-hydrolysis transition

217   state (Extended Data Fig. 4f). This implies that clamp-state MutS is able to hydrolyse and that

218   therefore it is not ATP that keeps the dimer clamped around the DNA, in agreement with recent

219   observation that Taq MutS can hydrolyse ATP in the clamp state [43]. Instead, it appears that it

220   is the DNA that keeps the dimer closed. In the sliding clamp structure, the lever domains of the

221   two monomers form an arc that surrounds the DNA duplex and interact with the DNA

222   backbone through numerous residues with a footprint of ~ 10 base pairs (Fig. 4a-b). In this

223   conformation the ATPase domains are closed, and the nucleotides trapped in the nucleotide

224   binding sites (Fig. 2c). Correspondingly, clamp-state MutS can only release the DNA at open

225   ends or single stranded DNA [18-21]. Large stretches of ssDNA are produced during downstream

226   events of the mismatch repair cascade through the action of A DNA helicase and DNA

227   exonucleases, which are likely to be encountered by clamp-state MutS, in contrast to double

228   strand breaks, that are not known to play a role in mismatch repair. To measure the minimal

229   length of the ssDNA gap needed to release clamp-state MutS from DNA, we used bio-layer

230   interferometry to measure the release from a DNA substrate containing a mismatch and

231   different sizes of ssDNA gaps in presence of 2 mM ATP (Fig. 4c). The dissociation rate of

232   MutS clamps increases with the size of the single stranded gap, from 0.02 s^{-1} on dsDNA or

233   nicked DNA until it reaches a plateau at 0.08 s^{-1} at a gap of 10 nucleotides or longer (Fig. 4d-

234   e). The ten-nucleotide gap is equal in size to the DNA footprint of the MutS dimer (Fig. 4b),

235   fitting with the notion that as the interactions with the dsDNA are lost, the dimer is no longer

236   able to remain clamped around the DNA and consequently falls off. Hence, by generating

237   ssDNA gaps, UvrD and exonuclease do not only remove the mismatch, but also generate a

238   simple release mechanism for MutS that would otherwise remain trapped on the DNA.

239

240

Discussion

DNA and ATP work together to coordinate the sequential steps of the repair cascade.

243   The four structures presented here provide a detailed view on the mechanism of ATP

244   hydrolysis and how the opening and closing of the dimer is at the core of the catalytic activity.

245   Combined with our recent structures of DNA-bound MutS during different stages of the repair

246   process [22], these new structures reveal how ATP hydrolysis and DNA binding co-operate to

247   coordinate the sequential steps of the mismatch repair pathway. In the absence of DNA, the

248   two MutS monomers freely open and close during ATP binding and hydrolysis (Fig. 5a). Due

249   to the alternating ATPase domains of MutS, only one ATP is bound by the dimer, preventing

250   it from assuming the most compact form, which is only reached with the non-hydrolysable

251   ATP analogues AMPPNP or ATPγS. When MutS associates with homoduplex DNA in search

252   for a mismatch, the DNA holds the dimer in an open form thus preventing ATP hydrolysis

253   (Fig. 5b). In this open conformation, the two nucleotide binding sites are freely accessible

254   enabling the loading of two ATP molecules. This open conformation of the ATPase domains

255   is retained when MutS first encounters a mismatch. However, mismatch binding induces a

256   small rearrangement of the clamp domains that acts as a licensing step that enable MutS to

257   transform into the sliding clamp [22] but not before both monomers bind ATP.

258   This transformation into the clamp-state involves a ~160° rotation of the mismatch and

259   connector domains of both monomers a ~ 20 Å translation of the DNA towards the centre of

260   the dimer as the lever domains cross each other firmly locking the DNA in the MutS clamp

261   (Fig. 5c) [22]. In the clamp state, the ATPase active sites are compatible with ATP hydrolysis,

262   yet due to the interactions between the MutS lever domains, the two monomers cannot open

263   up, presumably keeping the ADP-Pi trapped in the nucleotide binding site and preventing the

264   ATPase cycle to continue. Only when MutS encounters ssDNA, generated by UvrD and 5'-3'

265   or 3'-5' exonucleases during excision of the newly synthesized strand it is able to release itself

266   from the DNA and resume the hydrolysis cycle.

267   Thus, as the repair process continues, the size of the ssDNA is increased towards the

268   mismatch, reducing the time that MutS molecules reside on the DNA, until the mismatch is

269   removed and no more loading of MutS molecules takes place. Due to the low processivity of

270   UvrD in the absence of MutS and MutL, the excision of the DNA will soon cease after the

271   removal of a mismatch leaving the DNA open to be resynthesized by a DNA polymerase,

272   completing the repair process.

273

274

275   **Acknowledgement**

12

284

285   **Author contributions**

286   M.H.L. and A.B. conceived the overall experimental design; A.B. prepared samples,

287   collected and processed cryo-EM data; A.B. purified proteins and performed BLI experiments.

288   V.K. performed FRET experiments; A.B. and M.H.L. wrote the manuscript with contributions

289   from all authors.

290

291   **Competing interests**

292   The authors declare no competing interest.

293

294

295

296

297   **Methods**

298   **Materials**

299   All chemicals were purchased from Sigma Aldrich, unless indicated otherwise. All

300   chromatography columns were purchased from Cytiva.

301

Protein Expression and Purification

303   The dimeric version of *E. coli* MutS, R840E [36] was cloned into vector pETNKI-his3C-LIC-

304   amp [44]. Plasmids were transformed in *E. coli* BL21(DE3) pLysS cells and plated onto LB-agar

305   with 50 μg/ml chloramphenicol and 100 μg/ml ampicillin. All the colonies were scraped from

306   the plate and distributed over 6 x 500 ml Terrific Broth supplemented with 50 μg/ml

307   chloramphenicol, 100 μg/ml ampicillin, 1 mM $MgCl_2$ and 1% glucose. Cells were grown at

308   37°C to OD_{600} ~7, diluted with 1 volume Terrific Broth and induced with a final concentration

309   of 1 mM isopropyl 1-thio-β-D-galactopyranoside (IPTG) for 2 hrs at 30 °C. The proteins were

310   purified using a modified procedure from [45]. All subsequent steps were performed using basic

311   buffer (25 mM Hepes pH 7.5, 5mM MgCl2, 2 mM DTT) supplemented with NaCl or Imidazole

312   as indicated.

313   Harvested cells were resuspended in basic buffer with 500 mM NaCl and 10 mM imidazole

314   and lysed by sonication, followed by centrifugation at 14k x g. The supernatant was injected

315   onto a 5 ml HisTrap HP column and eluted with a gradient to 500 mM Imidazole in basic buffer

316   with 500 mM NaCl. Pooled fractions where diluted in ten volumes of basic buffer, injected

317   onto 5 ml HiTrap Heparin column and eluted with a gradient to 1 M NaCl in basic buffer.

318   Pooled fractions were concentrated and injected into a gel filtration column Superdex 200

319   16/600 equilibrated in basic buffer with 100 mM NaCl. Pooled fractions were injected onto a

320   5 ml HiTrap Q column equilibrated in the same buffer and eluted with a gradient to 1M NaCl

321   in basic buffer.

322

Cryo-EM sample preparation and imaging

Purified MutS was diluted to 4 µM in 20 mM Tris pH 8.5, NaCl 150 mM, 5mM MgCl2, 2 mM DTT and 0.01% (w/v) Tween 20. The diluted protein was incubated with 3 mM of either ADP, ATP, AMPPNP or ADP-Vi. Cu R1.2/1.3 or R2/1 holey carbon grids (Quantifoil, Groslöbichau, Germany) were glow discharged at 25 mA for 45 seconds using an Emitech K950 apparatus (Quorum, Laughton, United Kingdom). 3 µl of MutS-nucleotide sample were adsorbed onto glow-discharged grids and blotted for 1 second at 80% humidity at 4°C and flash frozen in liquid ethane using an EM GP plunge freezer (Leica). All cryo-EM data was collected at the The Netherlands Center for Electron Nanoscopy (NeCEN). The grids were loaded into a Titan Krios (FEI) electron microscope operating at 300 kV with a K2 or K3 direct electron detector equipped with a Bioquantum energy filter (Gatan, Pleasonton USA). The slit width of the energy filter was set to 20 eV. Images were recorded with EPU software (Thermo Fisher Scientific) in counting mode. Dose, magnification and effective pixel size are detailed in Table 1.

Cryo-EM image processing

All image processing was performed using Relion 3.1 [46]. The images were drift corrected using Relion's own (CPU-based) implementation of the UCSF Motioncor2 program, and defocus was estimated using gCTF [47]. LoG-based auto-picking was performed on a subset of micrographs and picked particles where 2D classified. Selected classes from the 2D classification were used as references to autopick particles from the full data sets. After two or three rounds of 2D classification, classes with different orientations were selected for initial model generation in Relion. The initial model was used as reference for 3D classification into different classes. The selected classes from 3D classification were subjected to 3D auto

347   refinement. The defocus values were further refined using CTF Refinement in Relion followed

348   by Bayesian polishing. Another round of 3D auto refinement was performed on these polished

349   particles. The density for MutS ADP-Vi was improved by using focused classification without

350   image alignment. All maps were post-processed to correct for modulation transfer function of

351   the detector and sharpened by applying a negative B factor, as determined automatically by

352   Relion. A soft mask was applied during post processing to generate FSC curves to yield maps

353   of average resolutions of 3.4 Å for MutS AMPPNP, 4.8 Å for MutS ADP, 3.8 Å for MutS

354   ADP-Vi and 3.3 Å for MutS ATP.

355   Model building was performed using Coot [48], REFMAC5 [49], the CCPEM-suite [50] and Phenix

356   [51]. For the ATP:ADP, AMPPNP$_2$ and ADPVi$_2$ structures we could build detailed model into

357   the high-resolution maps, while for the ADP$_2$ was limited to rigid body fitting of existing

358   structures and restrained refinement with REFMAC. Details on model refinement and

359   validation are in Table 1. In brief, model building started by rigid-body fitting known crystal

360   structures (PDB 1E3M and PDB 5AKB) into the different maps using Coot. Next, we carried

361   out one round of refinement in Refmac5 using jelly-body restraints, and the model was further

362   adjusted in Coot. After initial refinement, we generated improved-resolution EM maps using

363   the SuperEM method [52], which aided in model building and refinement. A final refinement

364   round and validation of the model and data were carried out using Refmac5 with proSmart

365   restraints within the CCPEM suite, with additional model validation using MolProbity within

366   Phenix.

367

368   **Negative stain EM sample preparation and imaging**

369   Purified MutS was diluted to 0.04 μM in 20 mM Tris pH 8.5, NaCl 150 mM, 5mM MgCl2,

370   2mM DTT, 0.01% Tween20 and 1 mM ADP. Grids were glow discharged 60 seconds at 25

371   mA using an EMITECH K950 apparatus. Three μl of sample were absorbed to glow-

372   discharged carbon-coated copper grids (C-Flat200-CU) and incubated for 30 s, before being

373   partially blotted. The grids were sequentially stained with three μl of 2.3% uranyl acetate,

374   incubated for 30 s and then blotted dry. Micrographs were collected on an FEI Tecnai Biotwin

375   electron microscope equipped with a LaB6 filament and operated at 120 kV and 49,000×

376   nominal magnification. The total dose was 20 e−/Å2 and the defocus values ranged from -0.5

377   to -3.0 μm. Images were collected with a FEI Eagle 4k x 4K CCD camera with final pixel size

378   of 4.44 Å.

379

380   **Negative stain image processing**

381   All image processing was performed using Relion 3.1 [46]. Contrast transfer function

382   estimation was performed with CTFFIND4.1 [53]. A small set of particles were manually picked,

383   2D classified and used as references for the auto picking procedure. 7845 particles were

384   extracted from a total of 73 micrographs. The extraction procedure was performed without

385   inverting contrast. Extracted particles were subjected to reference-free 2D average without

386   performing CTF correction.

387

388   **Biolayer Interferometry DNA substrates**

389   Six different DNA substrates with different gap lengths were prepared for the assays

390   (Supplementary Table 1). The substrates were prepared as follows: monovalent streptavidin

391   and a 5' biotinylated primer were mixed in a 1:1 ratio at a nominal concentration of 20 μM and

392   purified via analytical gel filtration using a Superdex 200 increase (3.2/30) column (Cytiva)

393   equilibrated in Tris 10 mM pH 8.0, NaCl 50 mM, EDTA 1mM. Fractions containing

394   biotinylated primer were mixed with the 5' biotinylated DNA template to create the final DNA

395   substrate. The efficient annealing of primer and template was confirmed with a 15%

396   polyacrylamide 0.5 x Tris Borate EDTA gel. Annealed substrates were stored at -20°C at a

397   concentration of 5 μM.

398

399   **Biolayer Interferometry DNA assay**

400   Association and dissociation kinetics between MutS and DNA were observed using the

401   Octet RED96 (Sartorius, Göttingen, Germany). All interactions studies were performed with

402   Streptavidin biosensors (Sartorius, Göttingen, Germany) conjugated to the biotinylate DNA

403   substrates. All the experiments were performed in the following buffer: Hepes 25 mM pH 7.5,

404   NaCl 150 mM, MgCl2 5mM, DTT 2mM, BSA 0.5 mg/ml, Tween 20 0.01%. The DNA

405   substrates were added in the loading step at 100 nM, until the threshold value of 0.36 nm was

406   reached. The association step was performed with MutS 200 nM in presence of 2 mM ATP.

407   The dissociation step was performed in buffer with 2mM ATP. Kinetic analysis were

408   performed using the Octet Data Analysis software package version 7.1.

409

410   **FRET assay**

411   Förster Resonance Energy Transfer (FRET) between labelled connector domain of one

412   subunit and the ATPase domain of the other subunit was measured using heterodimeric MutS

413   dimers similar as described before [36]. For labelling, proteins were diluted to 40 μM in 150 μl

414   of buffer (10 mM HEPES/KOH (pH 8.0), 200 mM KCl and 1 mM EDTA) and labelled with a

415   5-fold molar excess of Alexa Fluor 488 maleimide or Alexa Fluor 647 maleimide (Invitrogen,

416   Thermo Fisher Scientific, Waltham, MA) for 2 hours on ice in the dark according to the

417   manufacturer's instruction. Excessive dye was removed using Zeba Spin Desalting columns

418   (Thermo Fisher Scientific, Waltham, MA). The degree of labelling was determined from the

419   absorbance spectra recorded from 220–700 nm (nanodrop) according to the manufactures

420   instructions as described previously [36]. Heterodimers were allowed to form by mixing 10 μM

421   of MutS798C labelled with Alexa Fluor 488 and MutS246C labelled with Alexa Fluor 647,

422   and incubation on ice for at least 1.5 hours in the absence of nucleotides in buffer (25 mM

423   HEPES-KOH pH 7.5, 5 mM $MgCl_2$, 150 mM KCl, and 0.05 % (v/v) Tween 20). Aliquots of

424   the reaction were flash-frozen in liquid nitrogen and stored at -80 ºC. A 30-bp DNA substrate

425   with a central G:T mismatch was prepared by annealing T-strand (5' dig-

426   AATTGCACCGAGCTTGATCCTCGATGATCC-dig   3')   with   G-strand   (5'

427   GGATCATCGAGGATCGAGCTCGGTGCAATT 3'). Underlines mark the G:T mismatch.

428   The T-strand contains digoxigenin on either side, so that both DNA ends are blocked with 200

429   nM anti-digoxigenin Fab fragments (Roche Diagnostics, F. Hoffmann-La Roche Ltd,

430   Switzerland)

431   MutS heterodimers (50 nM monomer) were pre-incubated in 200 μl of FB150 buffer (25

432   mM HEPES-KOH pH 7.5, 5 mM $MgCl_2$, 150 mM KCl, and 0.05 % (v/v) Tween 20) in 96-

433   well plates at room temperature for 120 seconds. Next, 50 nM of the G:T DNA substrate was

434   added, followed by addition of 1 mM ATP, ADP, or AMPPNP (Jena Bioscience,

435   Jena, Germany, and AMPPNP from Sigma-Aldrich).

436   FRET was determined by measuring the fluorescence signals in microplate reader (TECAN

437   infinite F200, Tecan Group Ltd, Switzerland) before and 10 minutes later after the addition of

438   the dNTPs. Fluorescence signals were measured in three channels (donor, acceptor, FRET)

439   with the following filter combinations: (donor ex. 450 nm (width 20 nm) em. 535 nm (width

440   25 nm), acceptor ex. 620 nm (width 10 nm) em. 670 nm (width 25 nm), FRET ex. 485 nm

441   (width 20 mm) em. 670 nm (width 25 nm) filter.

442

Table 1 | Cryo-EM data collection, refinement and validation statistics				
	ADP	ATP:ADP	AMPPNP	ADP-Vi
Data collection and processing				
Magnification	x130,000	x105,000	x130,000	x130,000
Voltage (kV)	300	300	300	300
Electron exposure e$^-$/Å^2	57	54	54	34
Defocus range (μm)	-1 to -2.5	-0.5 to -2	-1 to -2.5	-0.5 to -2
Pixel size (Å)	1.06	0.866	1.06	0.66
Symmetry imposed	C1	C1	C1	C1
Initial particle images (no)	110,730	527,979	294,231	496,416
Final particle images (no)	41,730	151,672	147,899	81,316
Map resolution (Å)	4.8	3.3	3.4	3.8
FSC threshold	1.43	1.43	1.43	1.43
Map resolution range (Å)	4.5 to >10.7	3.3 to >4.8	3.4 to >4.3	3.7 to >6.9
Refinement				
Initial model used (PDB code)	1E3M	AMPPNP	1E3M	AMPPNP
Model resolution (Å)	7.8	3.6	3.4	4.0
FSC threshold	0.5	0.5	0.5	0.5
Map sharpening B factor (Å^2)	-50	-80	-80	-70
Model comparison				
Nonhydrogen atoms	10338	10955	10336	10800
Protein residues	1320	1393	1318	1373
B factors (Å^2)				
Protein	35-159	35-337	34-307	21-306
r.m.s deviations				
Bond lengths (Å^2)	0.013	0.012	0.014	0.013
Bond angles (°)	1.552	1.492	1.783	1.627
Validation				
MolProbity score	1.20	1.31	1.16	1.26
Clashscore	4.19	5.73	3.71	4.94
Poor rotamers (%)	0.09	0.96	0.00	0.09
Ramachandran plot				
Favored (%)	98.46	98.39	98.46	97.64
Allowed (%)	1.46	1.61	1.46	2.36
Disallowed (%)	0.08	0.00	0.08	0.00

443

Table 2 | Effect of mutations on the ATPase activity of *E. coli* MutS

Mutation	Reduction (fold)	Reference
Phe596Ala	2	Yang 2001
Lys620Ala	26	Haber 1991
Asp661Ala	1	Acharya 2008
Ser668Ala	4	Lamers 2004
Asn616Ala	5	Lamers 2004
His728Ala	25	Lamers 2004
Asp693Ala	22	Yang 2001

Reduction in ATPase activity compared to wild type MutS.

444

445

References

447

448   1.   Li, Z., Pearlman, A. H. & Hsieh, P. DNA mismatch repair and the DNA damage

449   response. *DNA Repair (Amst)* **38,** 94–101 (2016).

450   2.   Jiricny, J. Postreplicative mismatch repair. *Cold Spring Harb Perspect Biol* **5,** a012633

451   (2013).

452   3.   Welsh, K. M., Lu, A. L., Clark, S. & Modrich, P. Isolation and characterization of the

453   Escherichia coli mutH gene product. *J. Biol. Chem.* **262,** 15624–15629 (1987).

454   4.   Junop, M. S., Yang, W., Funchain, P., Clendenin, W. & Miller, J. H. In vitro and in

455   vivo studies of MutS, MutL and MutH mutants: correlation of mismatch repair and

456   DNA recombination. *DNA Repair (Amst)* **2,** 387–405 (2003).

457   5.   Hall, M. C. & Matson, S. W. The Escherichia coli MutL protein physically interacts

458   with MutH and stimulates the MutH-associated endonuclease activity. *J. Biol. Chem.*

459   **274,** 1306–1312 (1999).

460   6.   Kadyrov, F. A., Dzantiev, L., Constantin, N. & Modrich, P. Endonucleolytic function

461   of MutLalpha in human mismatch repair. *Cell* **126,** 297–308 (2006).

462   7.   Fukui, K., Nishida, M., Nakagawa, N., Masui, R. & Kuramitsu, S. Bound nucleotide

463   controls the endonuclease activity of mismatch repair enzyme MutL. *J. Biol. Chem.*

464   **283,** 12136–12145 (2008).

465   8.   Pluciennik, A. *et al.* PCNA function in the activation and strand direction of MutLα

466   endonuclease in mismatch repair. *Proc. Natl. Acad. Sci. USA* **107,** 16066–16071

467   (2010).

468   9.   Pillon, M. C., Miller, J. H. & Guarné, A. The endonuclease domain of MutL interacts

469   with the β sliding clamp. *DNA Repair (Amst)* **10,** 87–93 (2011).

470   10.   Yang, H., Yung, M., Sikavi, C. & Miller, J. H. The role of Bacillus anthracis RecD2

471   helicase in DNA mismatch repair. *DNA Repair (Amst)* **10,** 1121–1130 (2011).

472   11.   Walsh, B. W. *et al.* RecD2 helicase limits replication fork stress in Bacillus subtilis. *J.*

473   *Bacteriol.* **196,** 1359–1368 (2014).

474   12.   Burdett, V., Baitinger, C., Viswanathan, M., Lovett, S. T. & Modrich, P. In vivo

475   requirement for RecJ, ExoVII, ExoI, and ExoX in methyl-directed mismatch repair.

476   *Proc. Natl. Acad. Sci. USA* **98,** 6765–6770 (2001).

477   13.   Yamaguchi, M., Dao, V. & Modrich, P. MutS and MutL activate DNA helicase II in a

478   mismatch-dependent manner. *J. Biol. Chem.* **273,** 9197–9201 (1998).

479   14.   Lahue, R. S., Au, K. G. & Modrich, P. DNA mismatch correction in a defined system.

480   *Science* **245,** 160–164 (1989).

481   15.   Goellner, E. M., Putnam, C. D. & Kolodner, R. D. Exonuclease 1-dependent and

482   independent mismatch repair. *DNA Repair (Amst)* **32,** 24–32 (2015).

483   16.   Schofield, M. J., Nayak, S., Scott, T. H., Du, C. & Hsieh, P. Interaction of Escherichia

484   coli MutS and MutL at a DNA mismatch. **276,** 28291–28299 (2001).

485   17.   Acharya, S., Foster, P. L., Brooks, P. & Fishel, R. The coordinated functions of the E.

486   coli MutS and MutL proteins in mismatch repair. **12,** 233–246 (2003).

487   18.   Gradia, S. *et al.* hMSH2-hMSH6 forms a hydrolysis-independent sliding clamp on

488   mismatched DNA. **3,** 255–261 (1999).

489   19.   Blackwell, L. J., Bjornson, K. P., Allen, D. J. & Modrich, P. Distinct MutS DNA-

490   binding modes that are differentially modulated by ATP binding and hydrolysis. **276,**

491   34339–34347 (2001).

492   20.   Heo, S.-D., Cho, M., Ku, J. K. & Ban, C. Steady-state ATPase activity of E. coli MutS

493   modulated by its dissociation from heteroduplex DNA. *Biochem Biophys Res Commun*

494   **364,** 264–269 (2007).

495   21.   Jeong, C. *et al.* MutS switches between two fundamentally distinct clamps during

496   mismatch repair. *Nat. Struct. Mol. Biol.* (2011). doi:10.1038/nsmb.2009

497   22.   Fernandez-Leiro, R. *et al.* The selection process of licensing a DNA mismatch for

498   repair. *Nat. Struct. Mol. Biol.* **28,** 373–381 (2021).

499   23.   Hingorani, M. M. Mismatch binding, ADP–ATP exchange and intramolecular

500   signaling during mismatch repair. *DNA Repair (Amst)* **38,** 24–31 (2016).

501   24.   Davies, D. R. & Hol, W. G. J. The power of vanadate in crystallographic

502   investigations of phosphoryl transfer enzymes. *FEBS Lett.* **577,** 315–321 (2004).

503   25.   Groothuizen, F. S. *et al.* MutS/MutL crystal structure reveals that the MutS sliding

504   clamp loads MutL onto DNA. *Elife* **4,** e06744 (2015).

505   26.   Hopfner, K.-P. Invited review: Architectures and mechanisms of ATP binding cassette

506   proteins. *Biopolymers* **105,** 492–504 (2016).

507   27.   Hol, W. G. The role of the alpha-helix dipole in protein function and structure. *Prog*

508   *Biophys Mol Biol* **45,** 149–195 (1985).

509   28.   Hopfner, K.-P. & Tainer, J. A. Rad50/SMC proteins and ABC transporters: unifying

510   concepts from high-resolution structures. *Curr Opin Struct Biol* **13,** 249–255 (2003).

511   29.   Acharya, S. Mutations in the signature motif in MutS affect ATP-induced clamp

512   formation and mismatch repair. *Mol Microbiol* **69,** 1544–1559 (2008).

513   30.   Bjornson, K. P., Allen, D. J. & Modrich, P. Modulation of MutS ATP hydrolysis by

514   DNA cofactors. *Biochemistry* **39,** 3176–3183 (2000).

31. Antony, E. & Hingorani, M. M. Asymmetric ATP binding and hydrolysis activity of the Thermus aquaticus MutS dimer is key to modulation of its interactions with mismatched DNA. **43,** 13115–13128 (2004).

32. Lamers, M. H., Winterwerp, H. H. K. & Sixma, T. K. The alternating ATPase domains of MutS control DNA mismatch repair. **22,** 746–756 (2003).

33. Lamers, M. H. *et al.* ATP increases the affinity between MutS ATPase domains. Implications for ATP hydrolysis and conformational changes. **279,** 43879–43885 (2004).

34. Hopfner, K. P. *et al.* Structural biology of Rad50 ATPase: ATP-driven conformational control in DNA double-strand break repair and the ABC-ATPase superfamily. *Cell* **101,** 789–800 (2000).

35. Zhou, Y., Ojeda-May, P. & Pu, J. H-loop histidine catalyzes ATP hydrolysis in the E. coli ABC-transporter HlyB. *Phys. Chem. Chem. Phys.* **15,** 15811–15815 (2013).

36. Groothuizen, F. S. *et al.* Using stable MutS dimers and tetramers to quantitatively analyze DNA mismatch recognition and sliding clamp formation. *Nucleic Acids Res.* **41,** 8166–8181 (2013).

37. Mazur, D. J., Mendillo, M. L. & Kolodner, R. D. Inhibition of Msh6 ATPase activity by mispaired DNA induces a Msh2(ATP)-Msh6(ATP) state capable of hydrolysis-independent movement along DNA. *Mol. Cell* **22,** 39–49 (2006).

38. Iaccarino, I., Marra, G., Palombo, F. & Jiricny, J. hMSH2 and hMSH6 play distinct roles in mismatch binding and contribute differently to the ATPase activity of hMutSalpha. *EMBO J.* **17,** 2677–2686 (1998).

39. Studamire, B., Quach, T. & Alani, E. Saccharomyces cerevisiae Msh2p and Msh6p ATPase activities are both required during mismatch repair. *Mol Cell Biol* **18,** 7590–7601 (1998).

540 40. Sharma, A., Doucette, C., Biro, F. N. & Hingorani, M. M. Slow conformational

541   changes in MutS and DNA direct ordered transitions between mismatch search,

542   recognition and signaling of DNA repair. *J. Mol. Biol.* **425,** 4192–4205 (2013).

543 41. Monti, M. C. *et al.* Native mass spectrometry provides direct evidence for DNA

544   mismatch-induced regulation of asymmetric nucleotide binding in mismatch repair

545   protein MutS. *Nucleic Acids Res.* **39,** 8052–8064 (2011).

546 42. Gradia, S., Acharya, S. & Fishel, R. The human mismatch recognition complex

547   hMSH2-hMSH6 functions as a novel molecular switch. **91,** 995–1005 (1997).

548 43. Hao, P. *et al.* Recurrent mismatch binding by MutS mobile clamps on DNA localizes

549   repair complexes nearby. *Proc. Natl. Acad. Sci. USA* **117,** 17775–17784 (2020).

550 44. Luna-Vargas, M. P. A. *et al.* Enabling high-throughput ligation-independent cloning

551   and protein expression for the family of ubiquitin specific proteases. *J. Struct. Biol.*

552   **175,** 113–119 (2011).

553 45. Feng, G. & Winkler, M. E. Single-step purifications of His6-MutH, His6-MutL and

554   His6-MutS repair proteins of escherichia coli K-12. *BioTechniques* **19,** 956–965

555   (1995).

556 46. Zivanov, J. *et al.* New tools for automated high-resolution cryo-EM structure

557   determination in RELION-3. *Elife* **7,** 163 (2018).

558 47. Zhang, K. Gctf: Real-time CTF determination and correction. *J. Struct. Biol.* **193,** 1–12

559   (2016).

560 48. Emsley, P., Lohkamp, B., Scott, W. G. & Cowtan, K. Features and development of

561   Coot. *Acta Crystallogr. D Biol. Crystallogr.* **66,** 486–501 (2010).

562 49. Murshudov, G. N. *et al.* REFMAC5 for the refinement of macromolecular crystal

563   structures. *Acta Crystallogr. D Biol. Crystallogr.* **67,** 355–367 (2011).

564   50.   Nicholls, R. A., Tykac, M., Kovalevskiy, O. & Murshudov, G. N. Current approaches

565   for the fitting and refinement of atomic models into cryo-EM maps using CCP-EM.

566   *Acta Crystallogr D Struct Biol* **74,** 492–505 (2018).

567   51.   Liebschner, D. *et al.* Macromolecular structure determination using X-rays, neutrons

568   and electrons: recent developments in Phenix. *Acta Crystallogr D Struct Biol* **75,** 861–

569   877 (2019).

570   52.   Subramaniya, S. R. M. V., Terashi, G. & Kihara, D. **Super-Resolution Cryo-EM**

571   **Maps With 3D Deep Generative Networks**. *bioRxiv* 1–30 (2021).

572   doi:10.1101/2021.01.12.426430

573   53.   Rohou, A. & Grigorieff, N. CTFFIND4: Fast and accurate defocus estimation from

574   electron micrographs. *J. Struct. Biol.* **192,** 216–221 (2015).

575
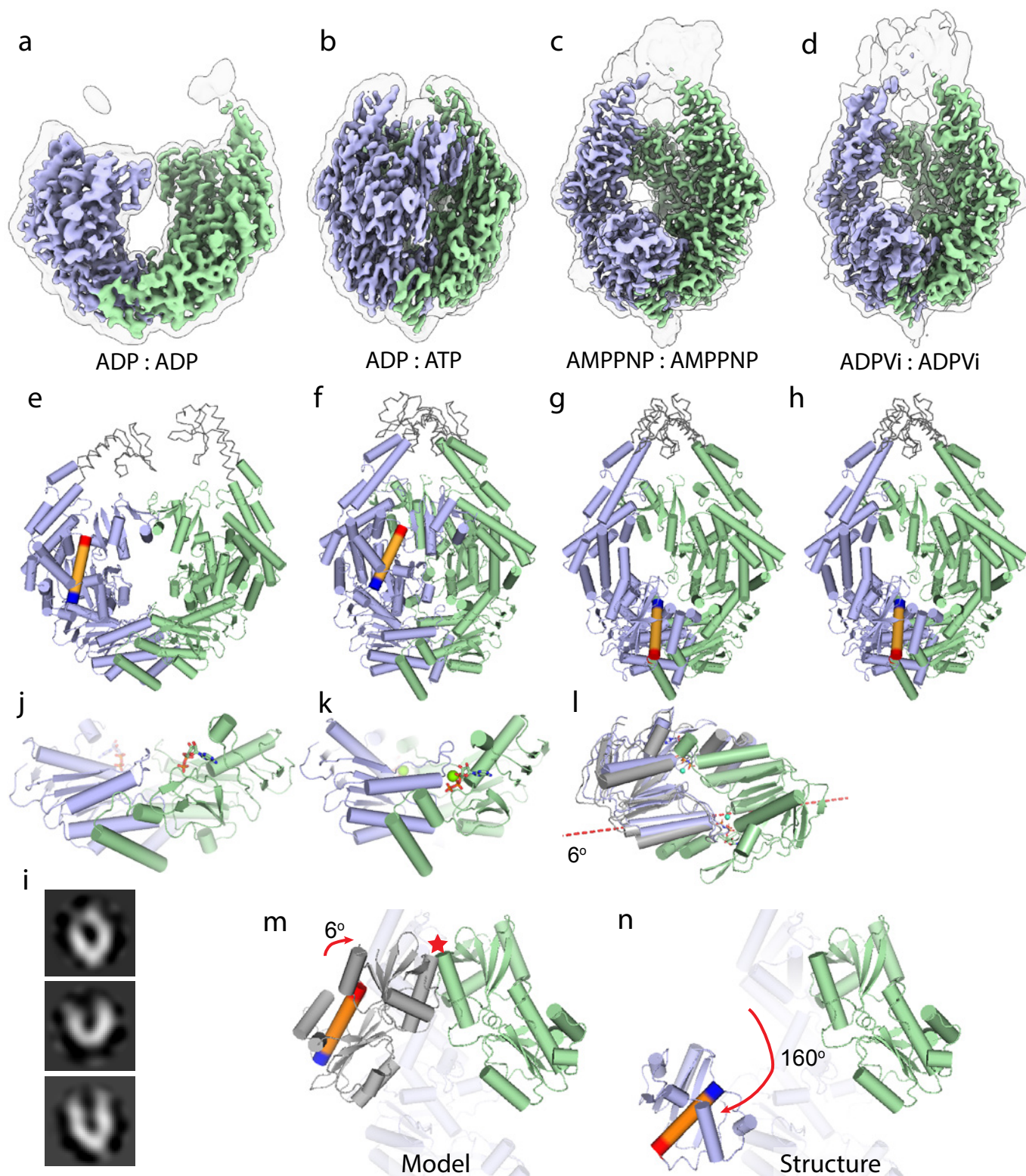
Fig. 1 | Structures of MutS at sequential steps of the ATP hydrolysis cycle. Cryo-EM maps of **a**, ADP-bound MutS, **b**, ATP-bound MutS, **c**, AMPPNP-bound MutS and **d**, ADP-Vi-bound MutS. Monomer A is shown in green, monomer B in blue. Transparent outlines show the same cryo-EM maps at lower contour level. **e-h**, Models of ADP, ATP, AMPPNP, and ADP-Vi bound MutS. Grey ribbon part of the models indicate approximate position of the missing clamp and lever domains that are poorly defined in the cryo-EM map. A central helix in the connector domain (residues 231 to 248) is colored in orange, with N- and C-termini colored in blue and red, respectively. **i**, Negative stain 2D classes of ADP-bound MutS showing the flexibility of the MutS dimer. **j-k**, Transition of the ATPase domains from ADP_2 to ATP:ADP-bound MutS that is a result of a 35° rotation of the two monomers. Yellow arrows indicate helix dipole that is attracted by the negative charge of the triphosphate in the opposite monomer. **k**, Transition of the ATPase domains from the ATP:ADP to $AMPPNP_2$-bound MutS. Grey model represent the original position of monomer B before the 6° rotation, dashed red line represents the rotation axis of monomer B. **m**, Model of the $AMPPNP_2$-bound MutS without the movement of the mismatch and connector domain. The red star indicated the clash the between mismatch binding domain of monomer A (coloured green) and monomer B (coloured grey). Core domain and ATPasee domain omitted for clarity. **n**, The rotation of mismatch and connector domain circumvents the clash with monomer A.
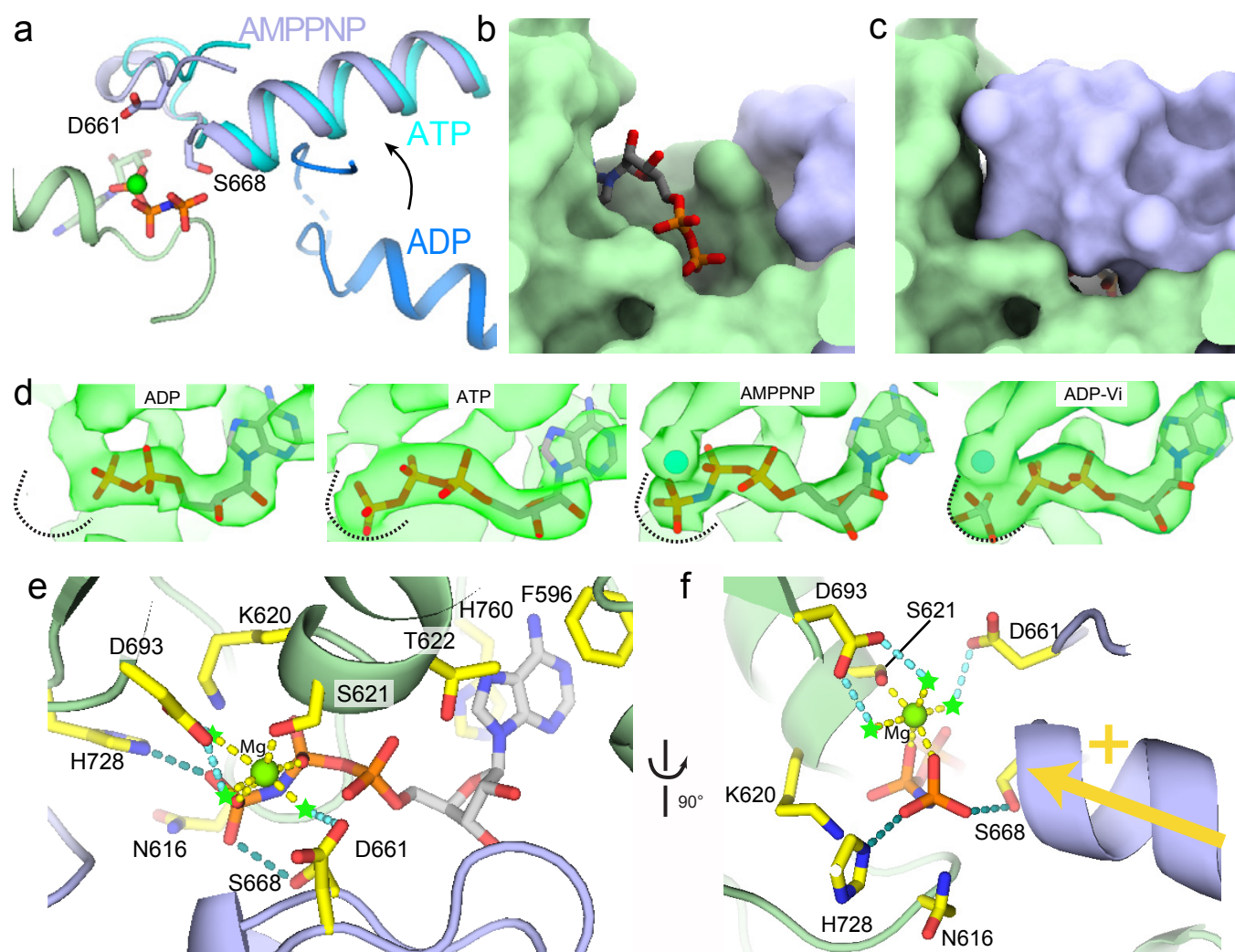
Fig. 2 | Closing of the MutS dimer completes the ATPase active site. a, Movement of the signature loop and helix of monomer B towards the nucleotide in monomer A. Monomer A in green, with AMPPNP and residues Asp661 and Ser668 shown as sticks. Monomer B in dark blue (ADP-bound), light blue (ATP-bound), and pale blue (AMPPNP-bound). **b**, Surface represenation of nucleotide binding site of ADP_2-bound MutS. Monomer A in green, monomer B in blue, and ADP molecule shown in sticks. **c**, Same representation for ATP:ADP-bound MutS. **d**, Close up of the cryo-EM maps at the nucleotide binding sites in ADP_2-, ATP:ADP-, $AMPPNP_2$-, and $ADP\text{-}Vi_2$-bound state. The dashed curved line show the boundary of the electron density map in the $ADP\text{-}Vi_2$-bound state. **e**, Close up of the composite ATP binding site showing the interactions with AMPPNP. Interacting residues are shown in yellow sticks and hydrogen bonds shown as dashed lines. Green stars mark predicted position of water molecules **f**, 90° rotation of the view shown in panel e.
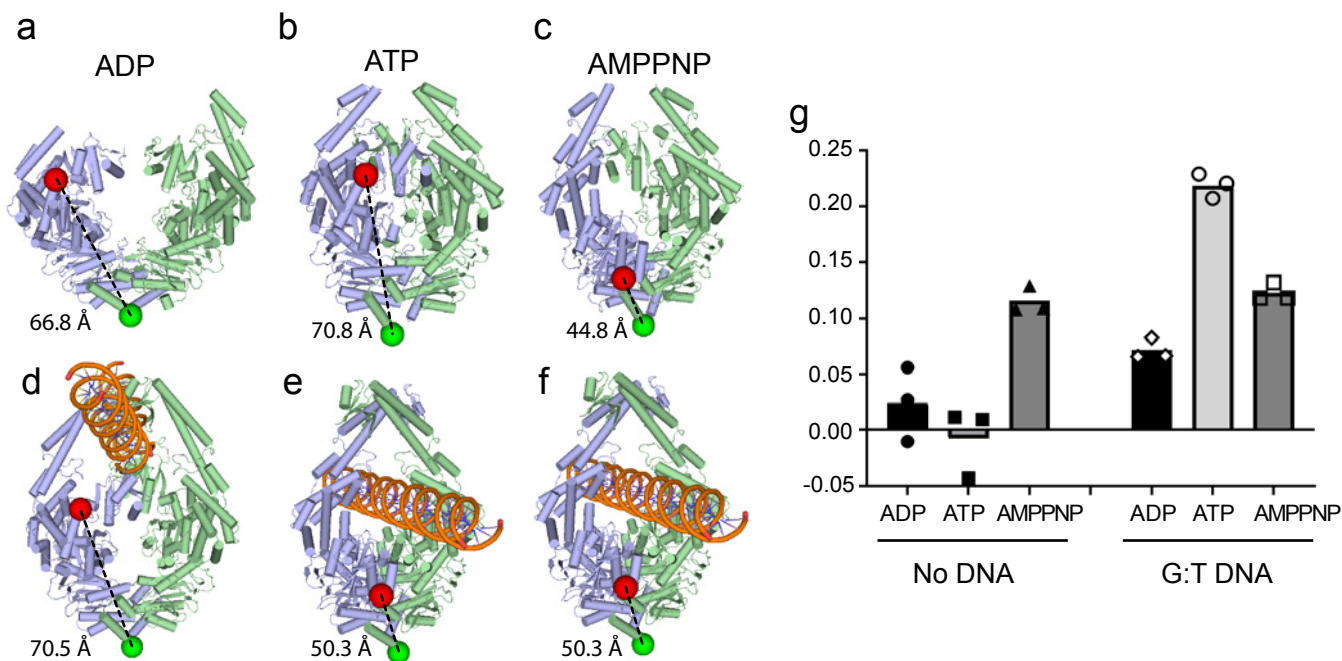
Fig. 3 | Two ATPs are needed for the MutS clamp formation. a-c, Structures of ADP_2, ATP:ADP, and AMP-PNP_2-bound MutS. Position of residues 246 and 798 are shown in red and green spheres, respectivily. **d-f**, Structures of DNA-bound MutS in presence of ADP, ATP, and AMPPNP [22]. **g**, Förster Resonance Energy Transfer (FRET) values between flurorescently labeled residues 246 and 798 in the presence of different nucleotides and DNA. Higher FRET values indicate a closer distance.
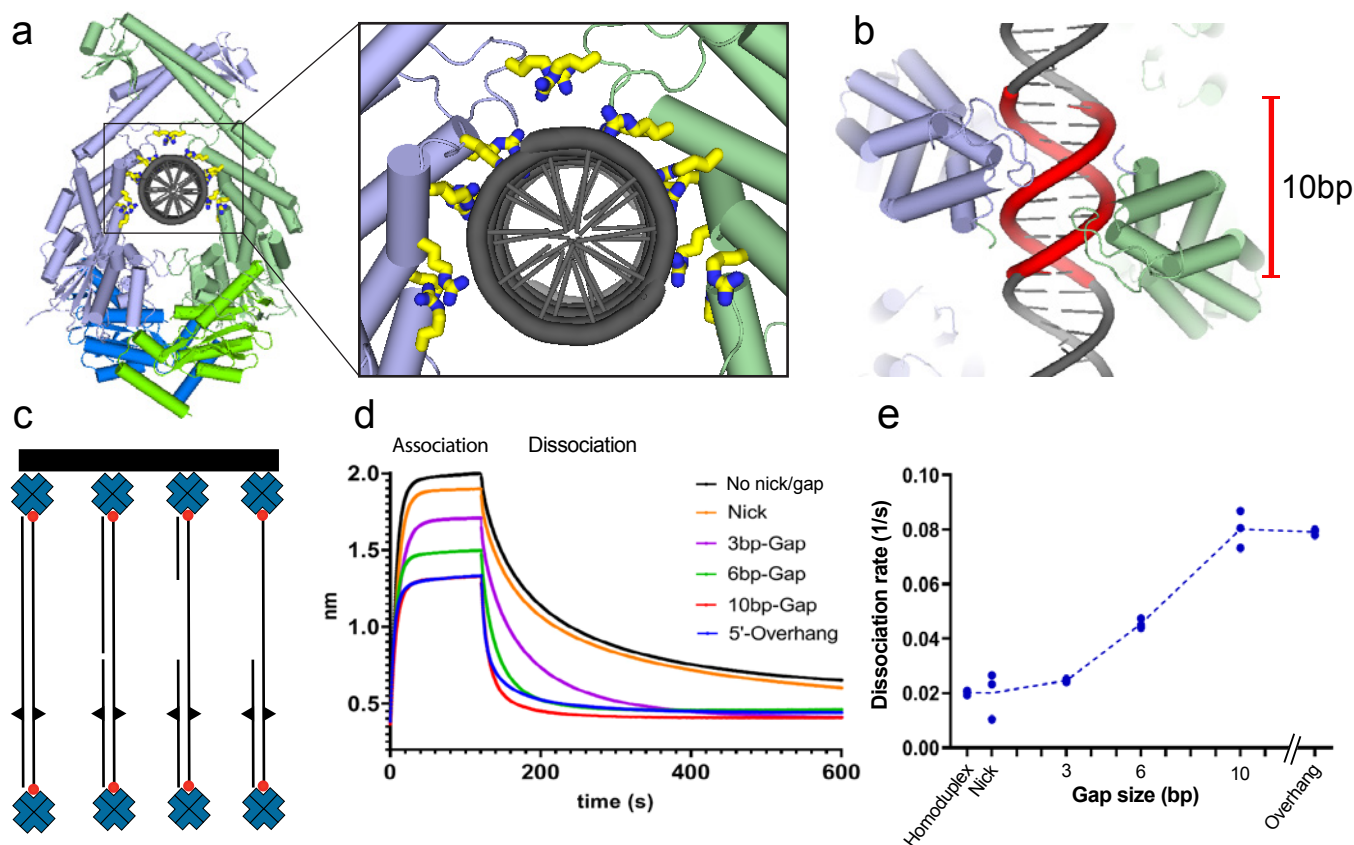
Fig. 4 | Release of MutS from DNA at a single stranded gap. a, Close-up of the protein-DNA interaction in the clamp state of MutS. Arginines and lysines that contact the DNA are shown in yellow sticks. **b**, Footprint of clamp-state MutS dimer on DNA covers 10 base pairs. **c**, Schematic representation of different DNA oligos used in the DNA release experiment. **d**, Association and dissociation of MutS on different DNA substrate in the presence of 2 mM ATP as measured by bio-layer interferometry. **e**, Dissocation rates derived from the binding curves shown in panel d. Dots mark rates calculated from three independent experiments.
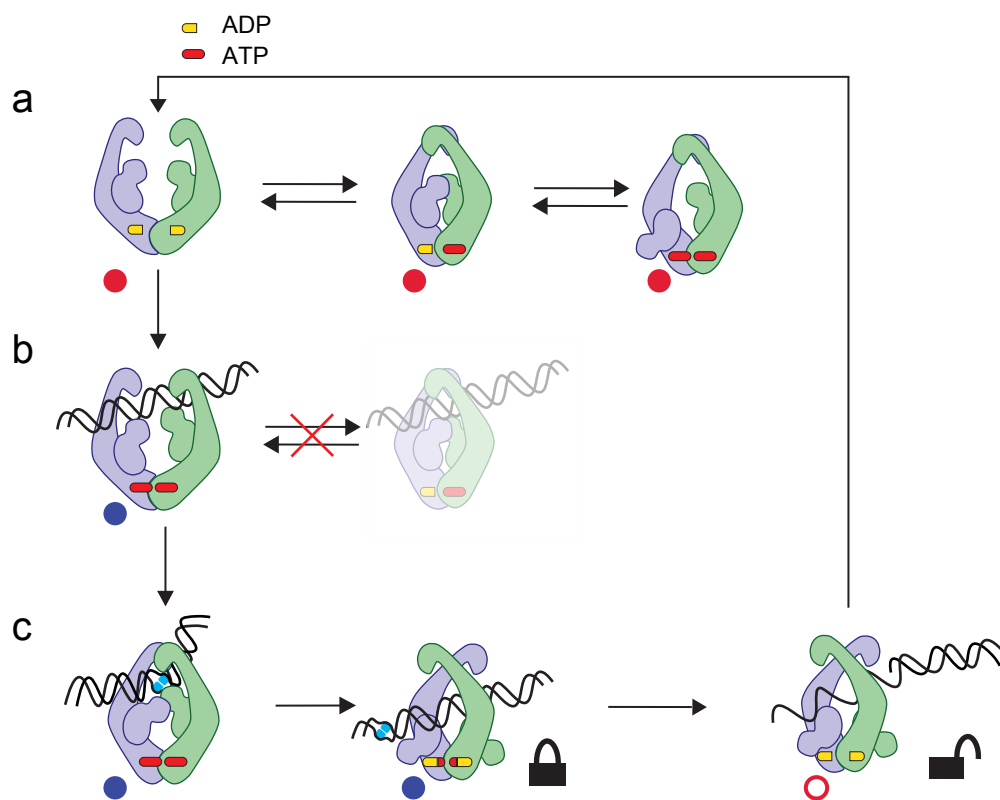
Fig. 5 | ATP and DNA co-operate to create sequential steps of the repair cascade. Cartoon style respresentation of the different steps of the DNA mismatch repair cascade derived from current and recent cryo-EM work. Red dots indicate structures presented in this work. Blue dots indicate cryo-EM structures presented in previous work [22]. Red circle indicate predicted structure based on data presented in Fig. 4. **a**, In absence of DNA, the two monomers can freely close and open upon ATP binding and hydrolysis. **b**, When bound to homoduplex DNA the MutS dimer can no longer close and is thereofore not able to hydrolyse ATP (indicated with faded cartoon). The open form of MutS on DNA can freely exchange ADP for ATP. **c**, Upon mismatch binding, MutS transforms into a sliding clamp that can hydrolyse ATP but is locked by double stranded DNA. Only upon encountering single stranded DNA, MutS can dissociate from the DNA and return to the open, ADP-bound form that can re-bind a new DNA substrate.
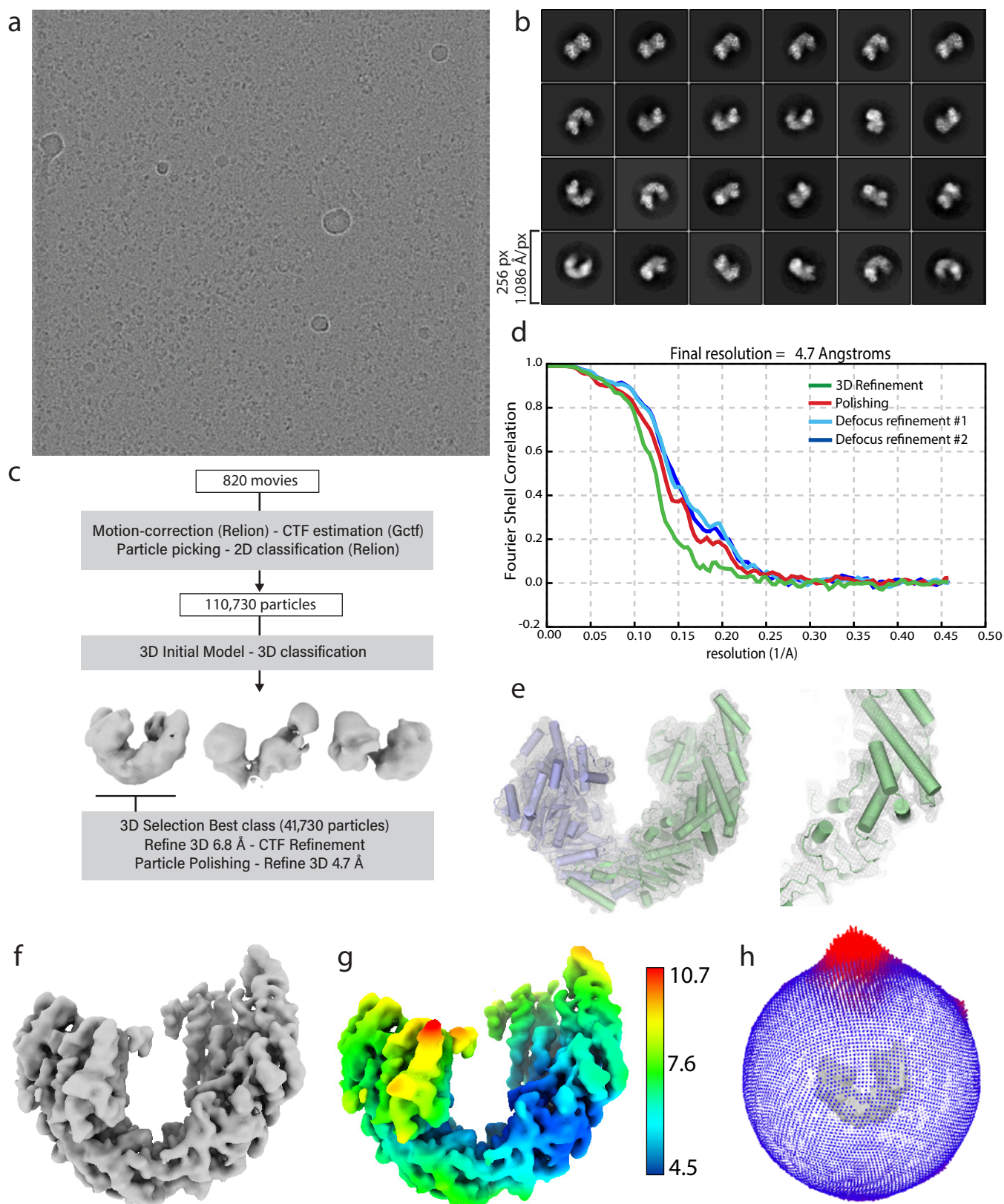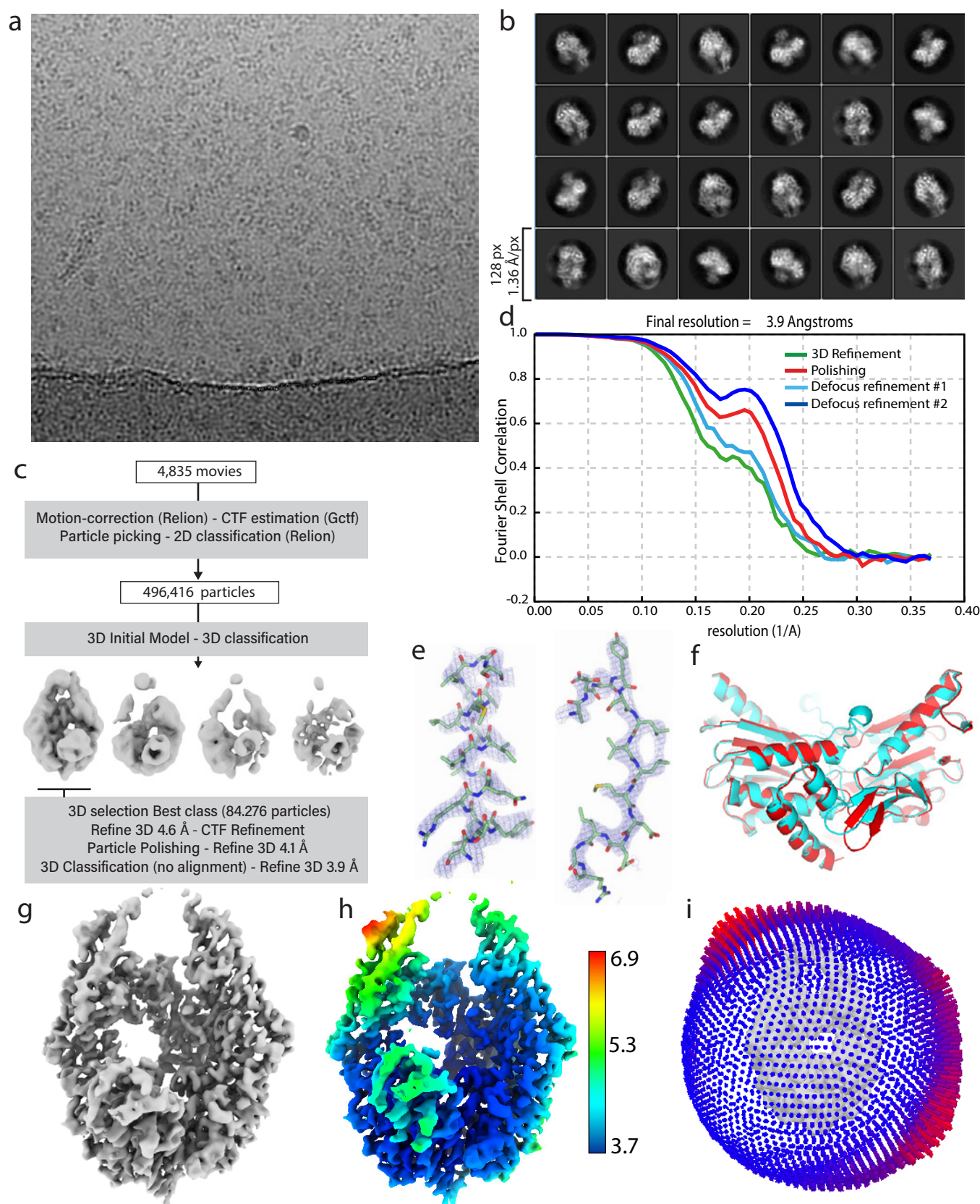
Extended Data Fig. 1 | CryoEM data analysis of ADP bound MutS. a, Representativ micrograph. **b**, 2D class averages from full dataset. **c**, Schematic representation of main data processing procedures. See methods section for more details. **d**, Fourier Shell Correlation between half-maps from subsequent refinements in the processing procedures. **e**, Detail of model fit to map. **f**, Final map obtained applying SuperEM code to Relion post-processed map. **g**, final map colored by local resolution. **h**, Orientation distribution in final set of refined particles.
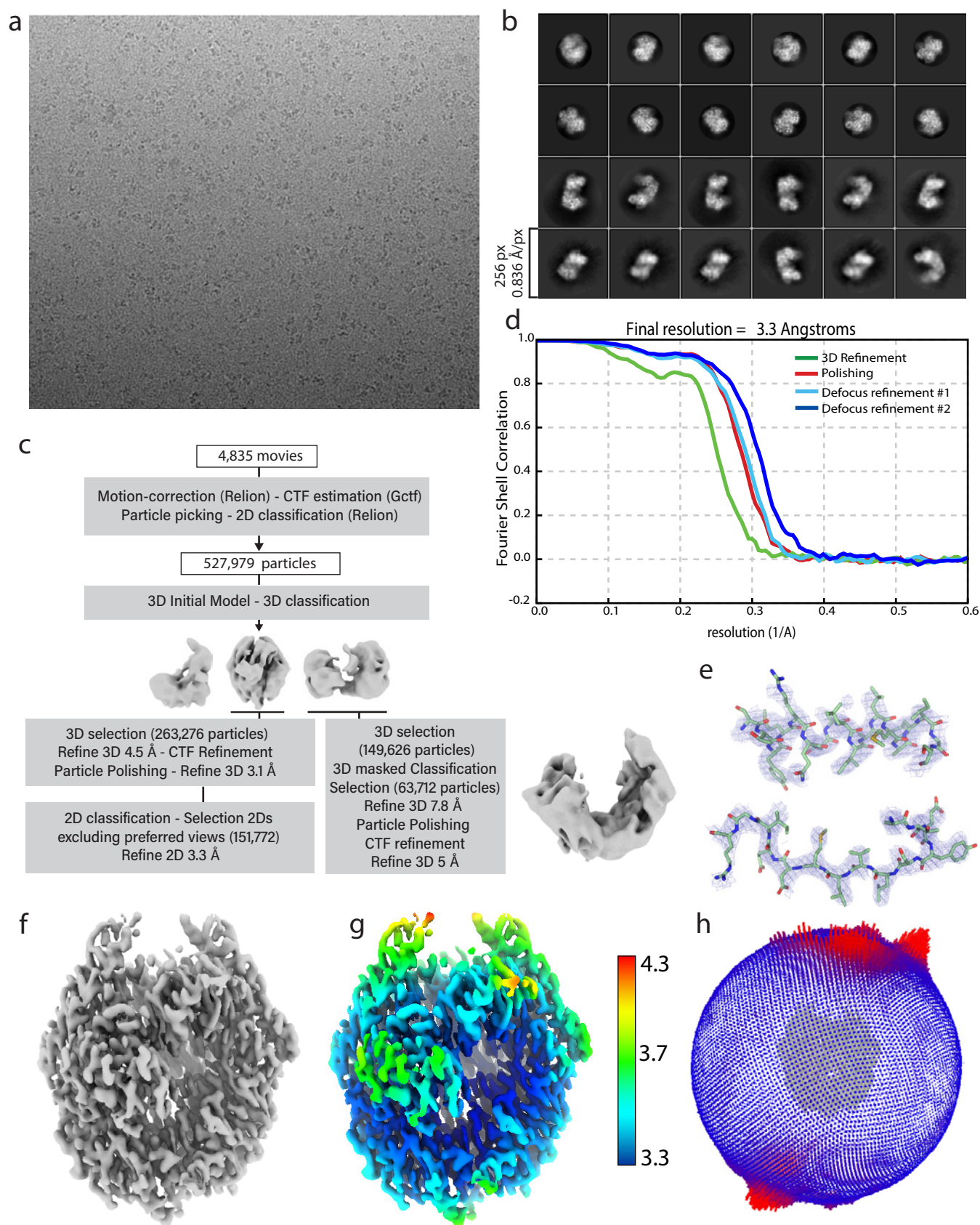
Extended Data Fig. 2 | CryoEM data analysis of ADP-ATP bound MutS. a, Representativ micrograph. **b**, 2D class averages from full dataset. **c**, Schematic representation of main data processing procedures. See methods section for more details. **d**, Fourier Shell Correlation between half-maps from subsequent refinements in the processing procedures. **e**, Detail of model fit to map. **f**, Final map obtained applying SuperEM code to Relion post-processed map. **g**, final map colored by local resolution. **h**, Orientation distribution in final set of refined particles.
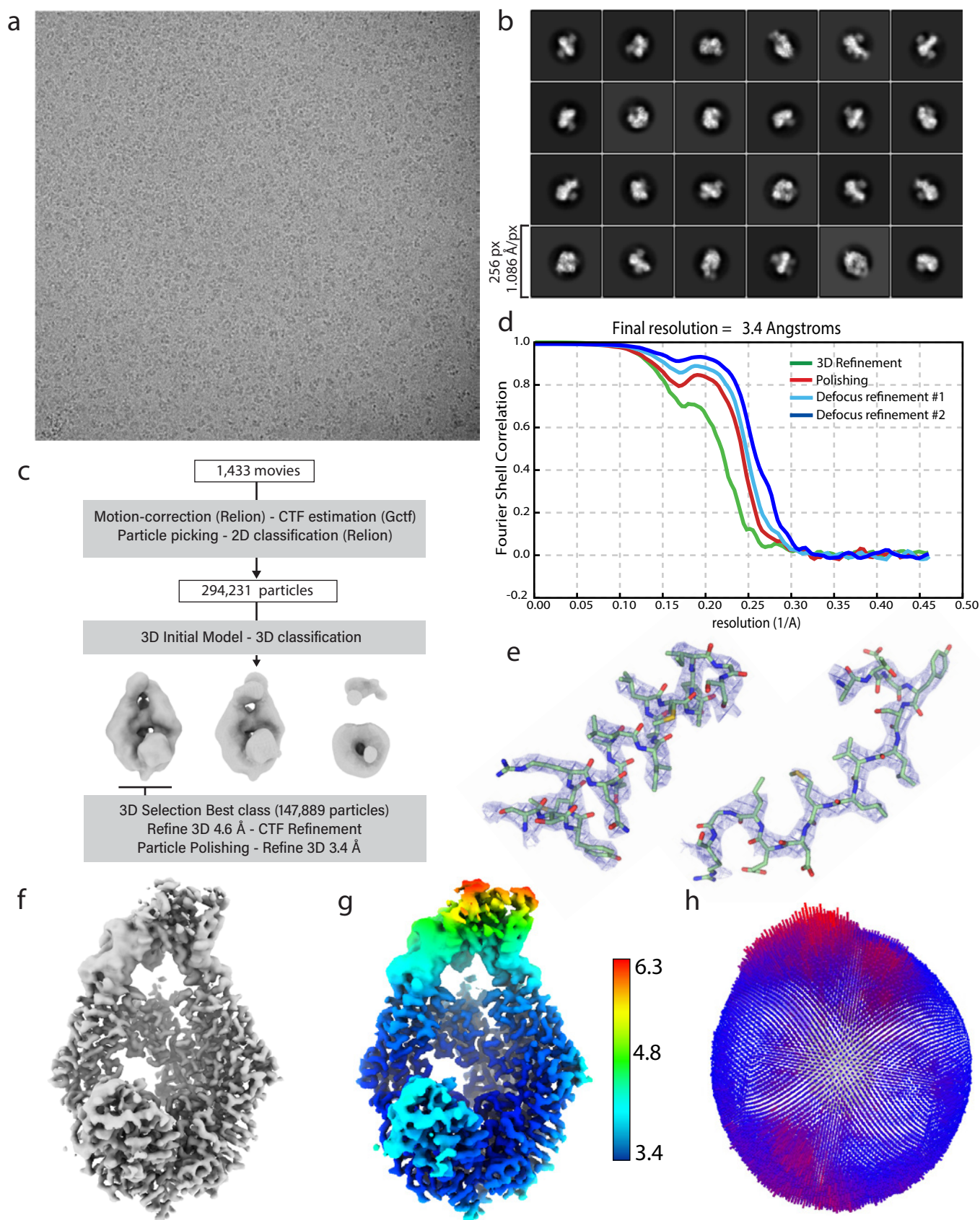
Extended Data Fig. 3 | CryoEM data analysis of ANPPNP bound MutS. a, Representativ micrograph. **b**, 2D class averages from full dataset. **c**, Schematic representation of main data processing procedures. See methods section for more details. **d**, Fourier Shell Correlation between half-maps from subsequent refinements in the processing procedures. **e**, Detail of model fit to map. **f**, Final map obtained applying SuperEM code to Relion post-processed map. **g**, final map colored by local resolution. **h**, Orientation distribution in final set of refined particles.

Extended Data Fig. 4 | CryoEM data analysis of ADP-Vi bound MutS. a, Representativ micrograph. **b**, 2D class averages from full dataset. **c**, Schematic representation of main data processing procedures. See methods section for more details. **d**, Fourier Shell Correlation between half-maps from subsequent refinements in the processing procedures. **e**, Detail of model fit to map. **f**, Superimposition of nucleotide binding domains of MutS in ADP-Vi conformation and MutS in sliding clamp MutL bound conformation (**Fernandez-Leiro 2021**). **g** Final map obtained applying SuperEM code to Relion post-processed map. **h**, final map colored by local resolution. **i**, Orientation distribution in final set of refined particles.